Fabrication of low aspect ratio three-element Boersch phase shifter for voltage-controlled three electron beam interference

Pooja Thakkar[1,2,*], Vitaliy Guzenko[3], Peng Han Lu[4], Rafal E. Dunin-Borkowski[4], Jan-Pieter Abrahams[1,2,5], and Soichiro Tsujino[1,2,**]

1. Division of Biology and Chemistry, Paul Scherrer Institut, CH-5232 Villigen PSI, Switzerland
2. Swiss Nanoscience Institute, University of Basel, Klingelbergstrasse 82, CH-4056 Basel, Switzerland
3. Photon Science Division, Paul Scherrer Institut, CH-5232 Villigen PSI, Switzerland
4. Ernnst Ruska-Centre for Microscopy and Spectroscopy with Electrons and Peter Grünberg Institute, Forchungszentrum Jülich, Wilhelm-Johnen-Strasse, 52428 Jülich, Germany
5. Biozentrum, University of Basel, Klingelbergstrasse 70, 4056 Basel, Switzerland

Abstract

A Boersch phase plate can shift the phase of electrons proportionally to the applied electrical potential, thereby allowing for *in-situ* control of the electron phase shift. A device comprising multiple of such phase shifter elements will be able to modulate the wavefront of a coherent electron beam and control electron interference. Recently, fabrication of single and 2x2 element Boersch phase shifter devices by focused ion beam have been reported, but realization of a large scale Boersch phase shifter array would demand further developments in device design and fabrication strategy e.g. by lithographic methods. Aiming at such a goal, we develop a fabrication method utilizing the state-of-the-art electron beam lithography and reactive ion etching, a combination which is widely used for high-throughput and large-scale micro- and nanofabrication of electronic and photonic devices. Using the developed method, we fabricated a three-element phase shifter with a metal-insulator-metal geometry and tested its electron transmission characteristics in a transmission electron microscope with the beam energy of 200 keV. The result showed the voltage-controlled evolution of electron interference, demonstrating the voltage-controlled electron phase shift of individual phase shifter element; π-phase shift was achieved by applying 1 V to the phase shifter element. We analyze the experimental results in comparison with 3-dimensional electrostatic simulation in terms of the phase-shift efficiency, the possible crosstalk between phase shifter elements and its elimination with a five-layer device structure.

* Electronic mail: pooja.thakkar@psi.ch
** Electronic mail: soichiro.tsujino@psi.ch

§1. Introduction

Holographic synthesis of electron waves via the phase front modulation has been actively studied recently[1–5]. Applications of the holographic electron wavefront control include the phase contrast enhancement of high-resolution microscopy[6–8], synthesis of vortex beam and higher order Laguerre-Gaussian beam with orbital angular momentum[1–3,5,9–14], Bessel beams[15], Airy beams[16], and the generation of arbitrary electron wave patterns in 2D[17] and 3D[4]. Such reported experiments demanded specialized static electron phase plates, that were designed via inverse modeling, fabrication, and insertion before or after the sample under investigation at a given microscope setting. The static phase plates are typically produced by nanofabrication methods such as the focused ion beam (FIB) milling[1,2] or electron beam lithography[4]. In contrast, a device, that allows for an active control of the local phase shift e.g. by applying voltage, will enable flexible use with in-situ tunability without adapting the phase plate parameters for specific microscope settings. In the case of Boersch phase plate[6–8,18–22], it is possible to operate the device with such flexibility. When an electron transmits through an aperture surrounded by a ring electrode, the phase of the electron is delayed or advanced by an amount proportional to the voltage applied to the electrode. Voltage-controlled phase modulating devices based on another approach have also been studied such as the nano-needle pair[9] and the nano-beam pair[11] for the purpose of producing electron vortex beams.

One of the interesting, and promising approaches is to use an array of the Boersch phase plate[20]. Such a device with sufficiently large number of phase shifter elements will be able to achieve the electron phase front modulation necessary for high-resolution microscopy and spectroscopy *in-situ* without the need to exchange the device and to readjust the observation conditions[20]. In analogy to liquid-crystal phase shifter array for visible light optics[23–26], such a device will extend the possibilities of electron wavefront engineering into practical applications in microscopy, diffraction analysis, and spectroscopic experiments. Matsumoto and Tonomura showed theoretically that the phase shift of the Boersch phase plate is uniform in the interior of the aperture[27]. Therefore, the calculation and programming for the electron wavefront synthesis will be straightforward with such a device. Even though up to 1000x1000 array of individually controlled electron beam array have been demonstrated for massively parallel electron beam lithography by splitting an electron beam incoherently[28–32], no such device exists yet for the coherent electron wavefront manipulation.

With the scalable and high-throughput fabrication of a large-scale phase shifter array as a goal, we are studying a fabrication method based on electron-beam lithography[4,13], which offers advantages of defining large-scale nanostructures with various materials, that can be also combined with subtractive and additive lithography processes[33,34]. In this work, we fabricate a three-element phase shifter device with metal-insulator-metal (MIM) 3-layer structure, a simplified device structure without one of the shielding electrodes, and test the electron transmission characteristics for a high energy coherent

electron beam in a transmission electron microscope equipped with a field emission electron gun. The successful observation of voltage-controlled electron interference demonstrated the phase shift capability of our device. In section 2, we describe the method of the device fabrication developed in this work. In section 3, we describe the experimental procedure for testing the phase shift performance of the fabricated device. In section 4, we present the experimental results on the voltage-controlled three beam interference, analyze the results in comparison with electrostatic simulation, and discuss the implications, and finally in section 5, we summarize and conclude.

§2. Device fabrication processes

Fig. 1a shows the schematic fabrication steps of the device. The schematic cross-section, the top-view optical image, and the top-view SEM image of the device are shown in Fig. 1b, c, and d, respectively. Our MIM device consists of three apertures through the insulator (~200 nm thick silicon nitride), that are individually surrounded by ring electrodes (~100 nm thick Au). The apertures and in turn the ring electrodes are arranged in a triangular geometry as shown in Fig. 1d. When an electron beam irradiates the device, electrons pass through apertures while electrical voltage V_n is applied to the ring electrode of the n-th phase element (PE-n, where n = 1, 2, 3) with respect to the bottom electrode (~50 nm thick Cr), that covers the entire bottom surface of the device chip. The diameter of the apertures and the center-to-center distance between adjacent apertures measured from the SEM image were respectively equal to 0.90±0.05 μm, and 1.8±0.05 μm. The width of the ring electrodes was equal to 280±20 nm and its inner circumference is offset by 80±10 nm from the aperture edges. The adjacent ring electrodes were separated by 120±10 nm.

The device chips are fabricated on a low-stress silicon nitride (SiN) membrane supported on a silicon substrate. The silicon layer underneath the SiN in the 150 μm square parts (marked in Fig. 1c) is removed, thereby the active part of the chip is built on the free-standing SiN membranes (Fig. 1a.1). To prepare the SiN membrane, a 200 nm thick SiN is first deposited on a 4" silicon wafer by low pressure chemical vapor deposition on both sides of the wafer. Next, ~500 μm square windows through the SiN layer are defined by photolithography and the reactive ion etching (RIE) on the back side of the wafer. Subsequently using the remaining SiN as the etching-mask the silicon layer is wet etched by a KOH solution at 70ºC resulting in ~150 μm big free-standing SiN membranes.

In the next step, Fig. 1a.2, we evaporate 50 nm thick chromium (Cr) on the back side of the chip by electron beam evaporation, which serves as the bottom electrode.

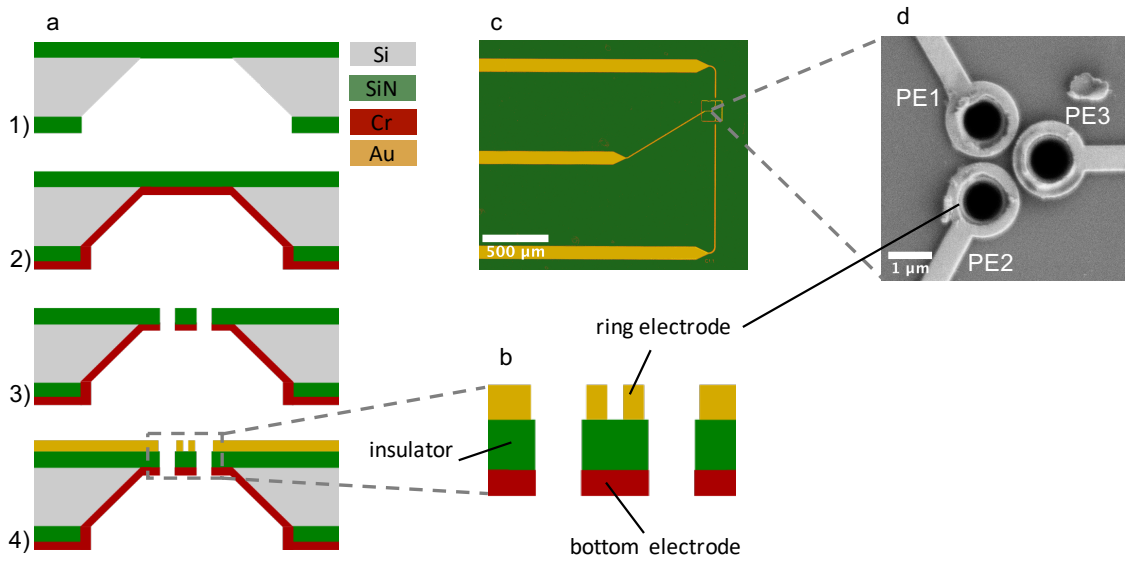

Figure 1: **(a)** A simplified schematic of fabrication process steps from top to bottom, 1. SiN membrane fabrication; 2. metal layer (Cr) evaporation on bottom side; 3. aperture patterning and transfer to all layers from membrane layer to Cr layer; 4. patterning of electrode rings around etched apertures **(b)** Schematic cross section of the Boersch phase shifter device. **(c)** Top-view optical microscope image (false colored) of the fabricated device. Three contact strips are connected to the three phase shifter elements PE1, 2, and 3, located in the squared area. **(d)** Top-view SEM image of the fabricated device. The three apertures with individual electrodes are located within the small square marked in (c)

In the subsequent step, Fig. 1a.3, the apertures through both SiN and Cr layers are fabricated. We pattern the resist mask (600 nm thick PMMA with the molecular weight of 950K) using an electron beam lithography tool (Vistec EBPG5000 PLusES 100kV). The SiN membrane is then etched by RIE (Oxford PlasmaPro 100) using the patterned PMMA as the etching mask. The gas mixture of CHF_3 (40 sccm) and Ar (25 sccm) is used to create plasma at 115 W RF power and 25 W ICP power, which gives an etching rate of ~10 nm/min . By avoiding O_2 gas mixture and adding Ar, the selectivity of the PMMA against SiN etching with the SiN etching rate equal to ~10 nm/min was achieved. To etch the underlying Cr layer, we transfer the chip to another RIE with chlorine chemistry (Bell Plasmatechnologie GmbH) with the gas mixture of Cl_2 (50 sccm) and O_2 (20 sccm) and etched for 2 min.

To achieve an alignment precision of ~5 nm between apertures and ring electrodes to be fabricated in the next step, six sets of rectangular alignment markers (70 nm thick Au) in two different sizes for coarse and fine alignment are fabricated in advance with electron beam lithography. The markers were chosen for each lithography step to ensure translational as well as rotational alignment.

In the last step, Fig. 1a.4, we fabricate the ring electrodes and their contact strips (Fig.1c). This is done by lift-off using a 400 nm thick PMMA (950K) as the positive mask. The PMMA mask is patterned by electron beam lithography. After the electron beam exposure and development of the resist mask, a ~7 nm thick Cr layer is deposited as the adhesion layer followed by a 100 nm thick Au layer, both by the electron beam evaporation method, on top of the patterned resist mask. The chip is subsequently dipped

into acetone to complete the lift-off of the metal layer evaporated on top of the unexposed resist. We added an offset of 80 nm between the edge of the apertures and the inner circumference of the ring electrodes for the purpose of supporting the resist layer over the apertures. This way, the metal deposition on the aperture sidewalls was prevented and the yield of the lift-off of the deposited metal layers was improved. Also, the dose for the resist exposure was optimized to improve the efficiency of the lift-off process e.g. by exposing ring electrode and connecting strips inside the membrane area at 1.5 times higher dose levels than peripheral, larger patterns such as contact strips and contact pads.

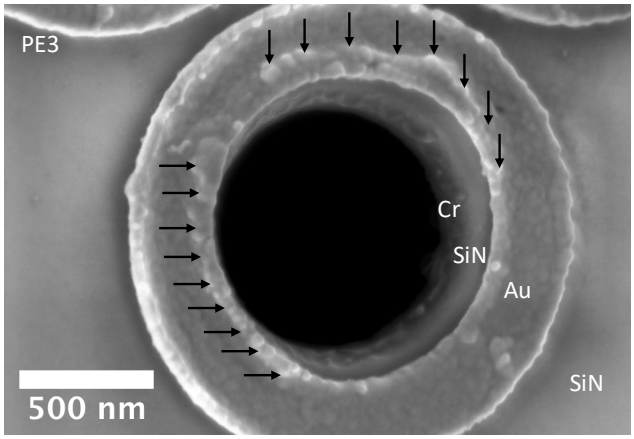

Figure 2: SEM image of phase shifting element PE3 taken at high magnification and a tilt of ~15°. The image shows a clean sidewall with insulated bottom (Cr) and ring electrodes (Au). The PE3 electrode showed an offset phase shift at 0 V which can be potentially due to error in the lift-off process which lead to a slightly thicker sidewall on parts of the ring electrode as can be seen from the image.

In Figure 2, we show a high magnification SEM images of the phase shifting element 3 (PE3) observed at 15° tilt angle. The sharp edge of the Au ring electrode and the smooth SiN sidewall inside the aperture are visible. The bottom electrode and the ring electrode are completely disconnected, owing to the self-aligned etching process of the SiN aperture and the Cr layer underneath. The electrical insulation between electrodes was confirmed in vacuum ($< 10^{-7}$ mbar) up to 20 V, which is an order of magnitude higher than the amount required to shift the phase by 2π as discussed below.

§3. Measurement of the phase shifter characteristics

The phase shift characteristics of the fabricated device were tested in FEI Titan G2 F20 field emission transmission electron microscope equipped with a CCD image sensor (EDAX r-TEM SUTW)[35] with the electron beam energy of 200 keV. The device chip was mounted on a holder with four electrical feedthroughs (DENSsolutions SH30) with the back side facing the beam source and inserted at the sample position of the microscope. A parallel electron beam was irradiated from the back side of the sample and the transmitted electron was imaged on the detector. The chip supporting plate of the holder, that was in electrical and mechanical contact with the backside of the chip, was biased at ~2 V as a protection of the microscope to avoid contacting the sample holder with pole piece. However, this did not contribute to the voltage differences between different PEs, hence unimportant to the interference of the electron beams transmitting through the apertures. The sample compartment was cooled by a liquid nitrogen bath to improve the vacuum. Therefore, the temperature of the device chip was reduced below ambient temperature.

In Fig. 3, the low-magnification transmission image of the device is shown, when all V_n's were set equal to 0 V. The three bright disks indicate that electrons transmitted the apertures of the three PEs unobstructed (transmission of 100 %). The dark rings and strips around the apertures show close to zero transmission through the Cr/Au layers of the ring electrodes. The transmittance of the electron beam outside the electrode area through 200 nm thick SiN and 50 nm thick Cr layers is equal to ~17% and low.

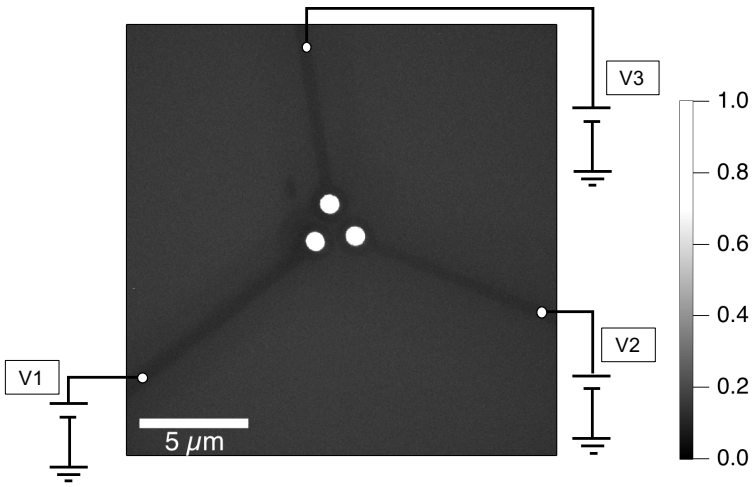

Figure 3: Low-magnification TEM image of the three-element Boersch phase-shifter device. Each phase shifter element was connected to a separate DC voltage source to apply the potential V_n (n = 1,2,3).

To observe the far-field interference pattern of electron beams passing through the device, we set the microscope in the diffraction mode with the weak excitation of the objective lens (approximately 5% comparing to ~80% in imaging mode) corresponding to an equivalent optical distance between the chip and the image detector equal to ~1400 m.

§4. Results and discussions

§4.1 Voltage-controlled three electron beam interference

In Fig. 4, we show the electron transmission images of the device acquired when the microscope was in the far-field diffraction mode. When V_n's applied to the PEs were equal to zero, Fig. 4a, we observed a hexagonal pattern of interference of three electron beams transmitted through three PEs. The central interference spot is the brightest as expected from the interference of three beams with equal propagation distances. The observation was reproduced by simulation Fig. 4d, wherein the simulated image was calculated by Fourier transform of three-aperture-image with the analogous size and geometry as our device. To match the simulation with experiment, the rotation of the three apertures was adjusted as shown in the insets in Fig. 4. The surrounding higher order diffraction spots are darker, since the finite aperture size of the PEs limits the angular spread of the transmitting electron beam within its Airy disk. The approximate cutoff of the interference pattern for the 2nd order and higher order diffraction spots is compatible with the ratio of the center-to-center separation of the phase elements (≈ 1.8 μm) to the diameter of the aperture (≈ 1 μm) approximately equal to 2.

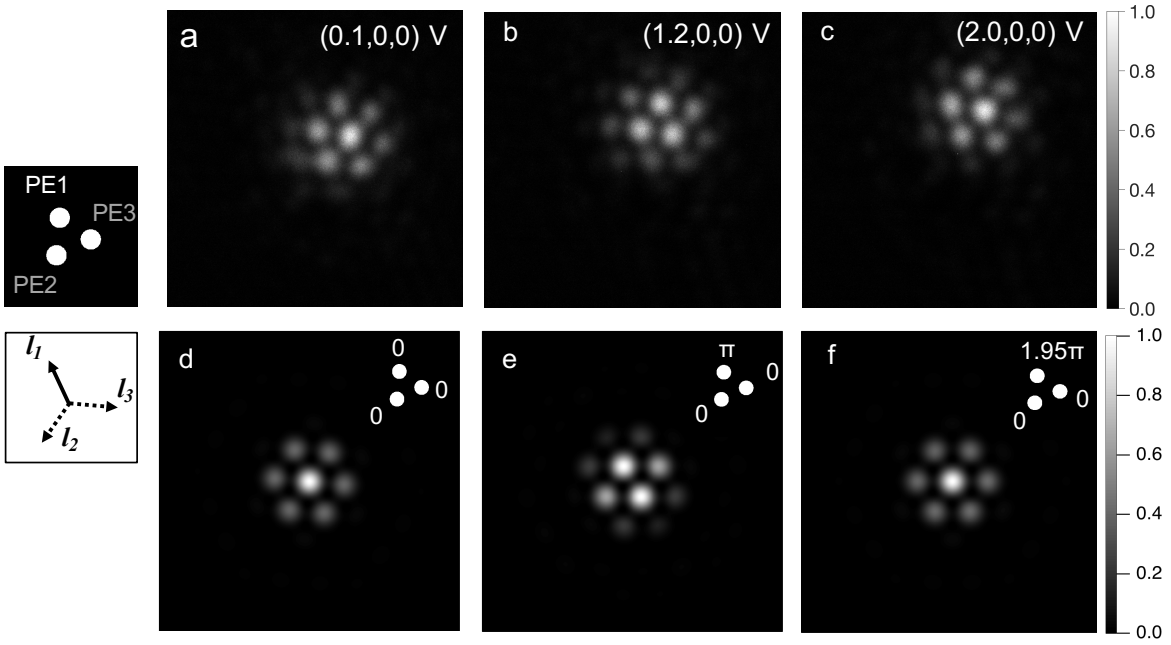

Figure 4: Voltage-controlled three-electron-beam interference, realized by the fabricated three-element Boersch phase-shifter device. The electron interference was observed using a 200 keV electron beam in a transmission electron microscope in the far-field diffraction setting. (a)-(c) shows the case when the voltage V_1 applied to the phase shifter element 1 (PE1) was equal to 0.1 V, +1.2 V, and +2 V, respectively, while setting voltages applied to PE2 and PE3 were equal to 0. (d-f) show the simulation calculated for the transmission phase of PE1 (right up aperture in the inset) was equal to 0, π, and 1.95π, respectively.

We next varied V_1 applied to PE1 in the range of -2 to 2 V while keeping $V_2 = V_3 = 0$ V. This changed the interference pattern (see Supplementary Video 1). The application of positive V_1 resulted in the shift of the interference spots in the l_1 direction (see inset at the left panel) i.e. toward PE1 from the middle

of the device as expected from the phase advancement of the beam through PE1 for positive V_1. When V_1 was increased from 0 V to 1.2 V, the interference spots shifted until the central part became a dark area sandwiched by two spots that were darker than the central spot at V_1 = 0.1 V. Comparing with the simulation, this is ascribed to the ~π phase shift of the electron beam passed through PE1 with respect to PE2 and PE3. Further increase of V_1 to 2 V continued to shift the interference spots until the image was same as the V_1 = 0.1 V case, indicating that the phase shift was approximately equal to 2π at this voltage, see Fig. 4f.

The same voltage-controlled variations of the interference patterns were observed when we applied voltages to PE2 as in the case of PE1, see Fig. 5a-c. We also observed a similar phase shift characteristics for PE3 but with a phase offset of ~0.5π (or ~ −1.5π), see Fig. 5d-f showing the case when V_3 = 1.2, 2.0, and 2.8 V, that correspond to the phase shifts approximately equal to 0, π, and 2π, respectively. Although the phase offset of PE3 is significant, it could be compensated by applying a small voltage as shown here. The origin of the offset is tentatively ascribed to charging around the aperture but yet to be elucidated.

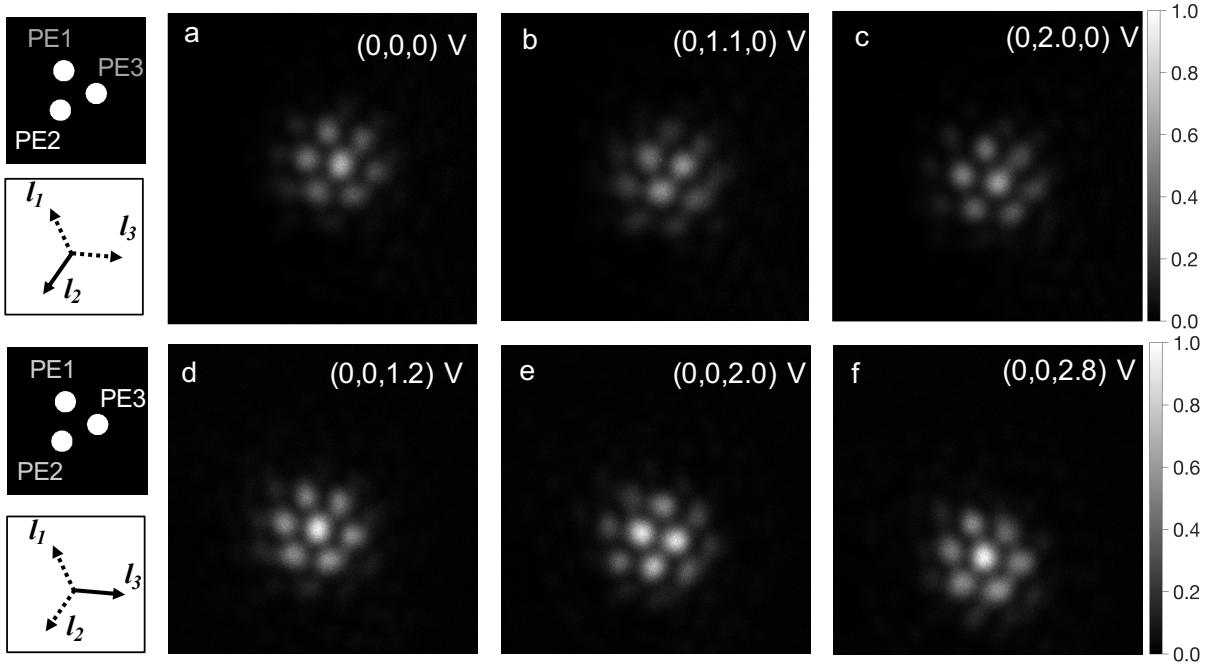

Figure 5: Observed far-field diffraction pattern of PE2 and PE3 at **(a)** (0, 0, 0) V, **(b)** (0, 1.1, 0) V and **(c)** (0, 2.0, 0) V; and **(d)** (0, 0, 1.2) V, **(e)** (0, 0, 2.0) V and **(f)** (0, 0, 2.8) V.

To analyze the observed voltage-controlled electron beam interference and the phase shift in detail, we extracted the intensity cross-sections of the interference images along the lines going through the center of the interference images in the directions of l_n's (n = 1,2,3) shown in Fig. 4. In Fig. 6a we show the result of the analysis at the selected voltages for the dataset when V_1 was scanned. The dashed curves show the simulation calculated with phase shifts that gave the same sidelobe intensity ratios. In Fig. 6b

and c, we show the result of the analysis for the datasets when V_2 and V_3 were scanned, respectively. The zero-bias intensity profile of the V1-scan data showed an asymmetry, suggesting a small voltage offset. A larger voltage offset was observed for the V3-scan dataset as already indicated in Fig. 5.

In Fig. 7, we summarize the relationship between the bias voltage and the phase shift at each V_n's evaluated from the fitting for the three datasets. We found that the phase shift characteristics of PE1 and PE2 are same as indicated by the black dashed line with the slope and the phase offset equal to 1.07 ± 0.02 π rad/V and - 0.13π, respectively. The red dashed curve shows the linear fit for the PE3 case, with the phase offset of -1.3 π. Nevertheless, its slope equal to 1.14 ± 0.04 π rad/V was found to be equal to that of the phase shift characteristics of PE1 and PE2 within 6 %.

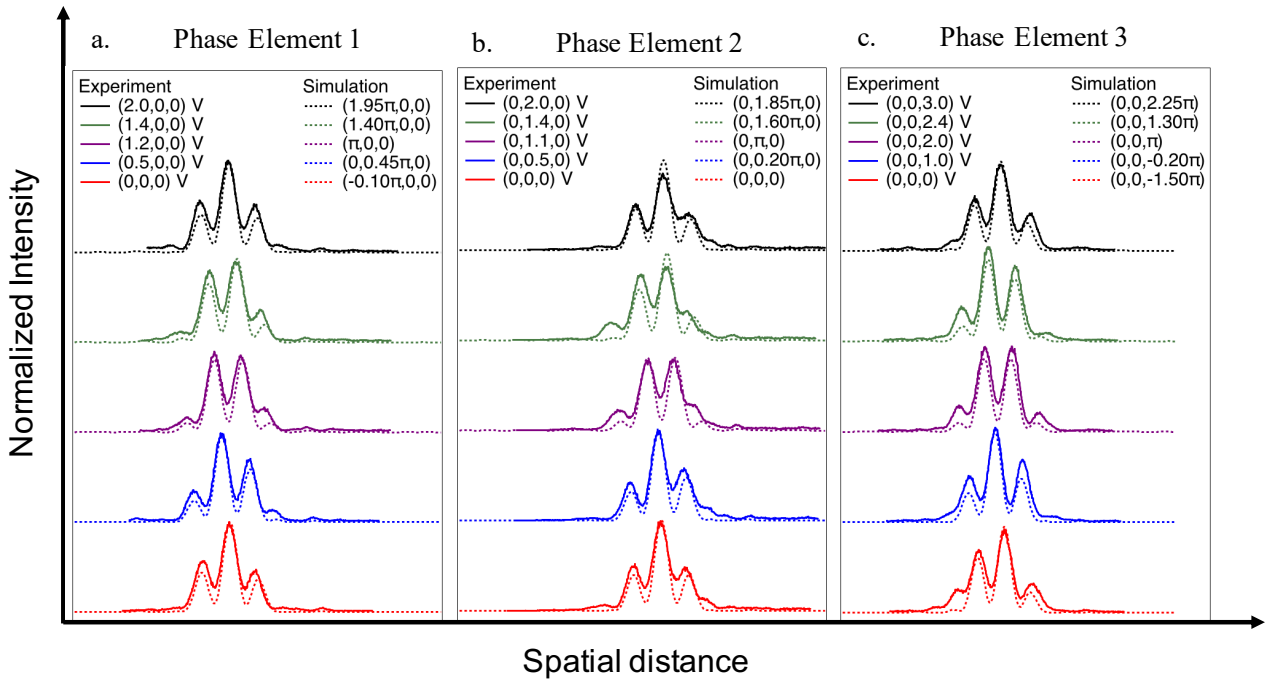

Figure 6: Fitting of line profiles of experimentally observed diffraction patterns (0V - 2V) for PE1 and PE2 and (0V – 3V) for PE3 with simulated diffraction patterns (0 – 2.5π), voltage induced drift between consecutive curves is linearly compensated. PE1 and PE2 can shift phase of electron by π at an applied voltage of approximately 1V.

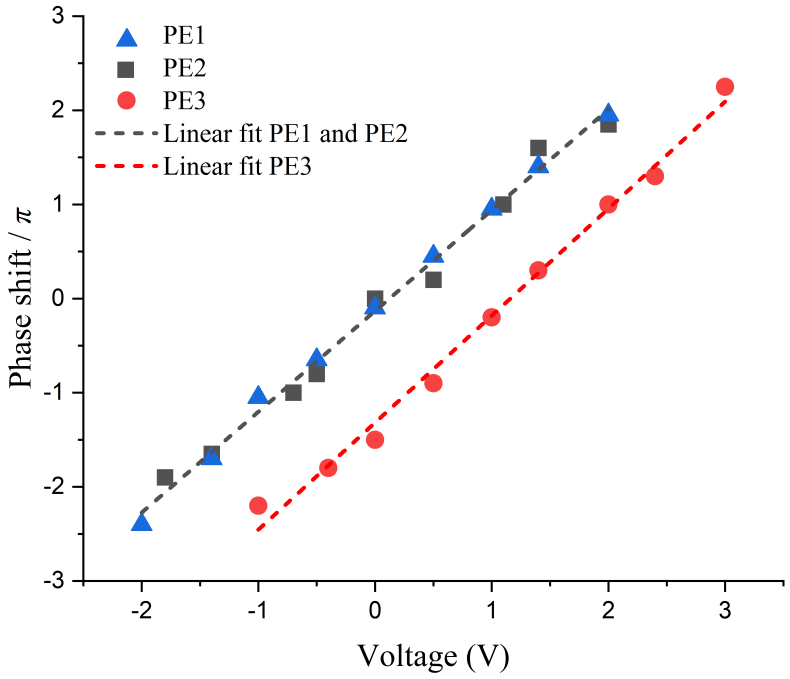

Figure 7: Phase shift vs applied voltage plotted for Phase element 1 (PE1), PE2 and PE3. The intensity cross-sections of observed diffraction patterns is fitted with analytically calculated phase shifts for randomly chosen patterns between -2 V to 3 V. The phase shift is linearly related to the applied voltage for all three PEs. PE3 needs an increased amount of voltage for similar phase shift compared to PE1 and PE2.

§4.2 Vortex beam generation using three phase shifting elements

Next we applied voltages to the three phase shifter elements to set the phase shift for PE1 and 2 with respect to PE3 equal to $-2\pi/3$, $2\pi/3$, and 0, respectively, that takes into account the phase offset of PE3. This condition leads to the three-beam approximation of the vortex beam with the orbital angular momentum of $1\hbar$. Fig. 8a shows the result. The central dark spot surrounded by three spots with the same brightness indicates the vortex singularity. The observation in Fig. 8a compares well with the simulation shown in Fig. 8b. Although the three-beam approximation is rather rudimentary, the inline formation of the vortex beam instead of the finite order diffraction is potentially advantageous for applications in terms of the beam brightness and the alignment on the sample.

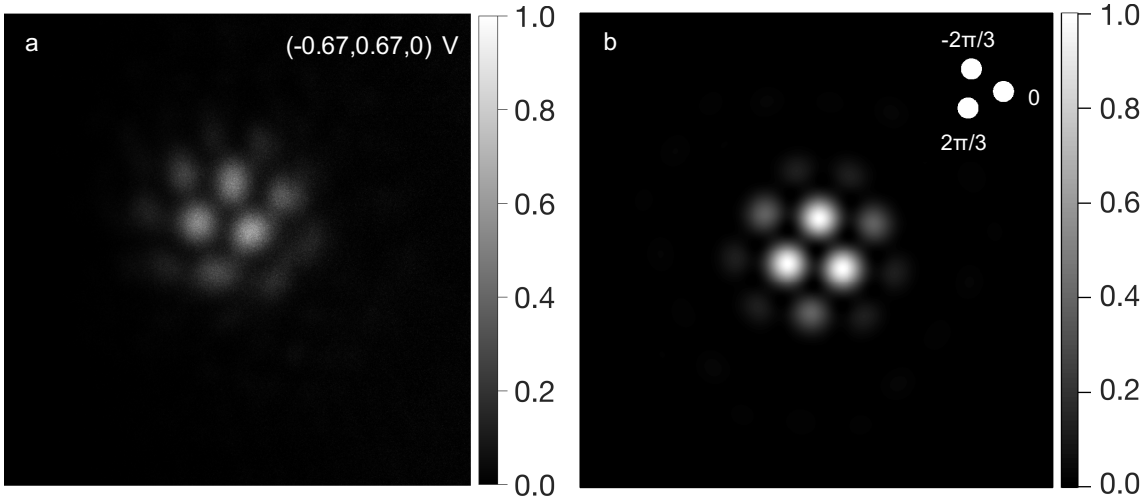

Figure 8: ***(a)*** *Vortex beam singularity for (-0.67,0.67,0) V generated with only three individually controlled phase elements (b) corresponding FFT simulation*

§4.3 Comparison with 3-dimensional electrostatic simulation

Now we compare our experiment with an electrostatic simulation. In the Boersch phase shifter, when an electron propagates through the aperture, the electron phase is advanced by an amount proportional to the DC voltage V_E applied to the ring electrode with the thickness of t_E surrounding the aperture. The ring electrode is sandwiched by a pair of electrodes at ground potential at the top and bottom, thereby the electron energy of the incident and transmitted beam are same [7,18,19]. Assuming that the potential inside the phase shifter aperture varies stepwise between 0 and V_E within the thickness t_E of the ring electrode as in the case when the electron propagates through a material with the potential of V_E, the phase shift $\Delta\phi$ is given by $\sigma V_E t_E$. The coefficient σ is given by the following equation when the kinetic energy E (in the order of the electron rest mass energy E_0) is much larger than V_E [36],

$$\sigma = \frac{2\pi}{\lambda}\frac{E+E_0}{E(E+2E_0)}. \qquad (1)$$

In Eq. (1), λ is the electron wavelength. For a 200 keV electron beam (E = 200 keV), λ = 2.5 pm and σ is equal to ~7.29×10^6 rad V^{-1} m^{-1}.

The variation of the potential along the beam trajectory in the actual device varies gradually. Therefore, the maximum voltage and the (effective) width of the potential depend on the electron trajectory i.e. if the electron propagates at the center or near the edge of the phase shifter aperture because of the different distance from the ring electrode. However, the influence of this on the phase shift is negligible as demonstrated by Matsumoto and Tonomura[27]: the phase shift $\Delta\phi$ for an electron that propagates through the aperture, which is given by the following integral, does not depend on the location (x,y) within the aperture of the electron trajectory,

$$\Delta\phi = \sigma \int_{-\infty}^{\infty} U(x,y,z)dz \ ; \qquad (2)$$

where $U(x,y,z)$ is the potential distribution produced by the phase shifter element (the x-y plane is parallel and the z-direction is perpendicular to the sample plane and parallel to the electron trajectory). The z-dependence of the potential distribution and $\Delta\phi$ deviate from the stepwise potential variation, especially in our geometry wherein one of the electrodes sandwiching the ring electrode is omitted.

For a quantitative comparison with experiment, we calculated the three-dimensional electrostatic potential distribution of our device by a finite element solver (COMSOL Multiphysics) and evaluated the phase shift by Eq. (2). We assumed the same size and geometry for the three PEs as the fabricated device. First we discuss the result of the simulation without contact strips. The influence of the contact strips is discussed in the next section.

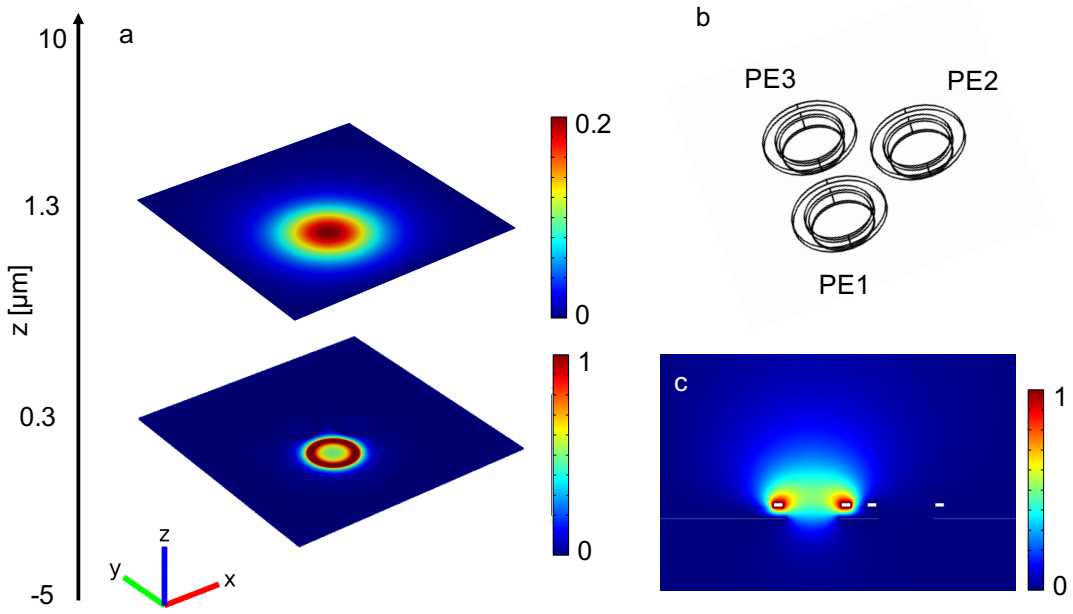

Figure 9: The calculated potential distribution of the three-aperture system metal-insulator-metal (MIM) device with phase shifting element 1 (PE1), PE2 and PE3 is shown in (b). The voltage distribution of the MIM device at z = 0 µm and z = 1 µm are shown in (a) when V_1 = 1 V (potential values are normalized to maximum (red) for all images). From the cross-section of the MIM device in (c), the crosstalk between two neighboring elements can be understood by the unscreened potential due to missing top electrode.

In Fig. 9, we show the calculated potential distribution when V_1 = 1 V, and $V_2 = V_3$ = 0 V. The bottom electrode surface lies along the x-y plane at with z = 0 µm, and the ring electrodes reside above, see Fig. 9c. Fig. 9a shows the potential distribution along the plane parallel to x-y plane at z = 0.30 µm (at the surface of the top electrode) and at z = 1.3 µm (1 µm above the ring electrode), respectively. Figs. 9a and c show that the potential beneath the bottom electrode goes to zero sharply but elongated in the positive z direction more than 1 µm above the ring electrode. See also Fig. 10a depicting the potential variation along the selected trajectories. Lc is the case when the electron trajectory is long the center of

PE1. The width of the potential along trajectories as determined by the integral in Eq. (2) is equal to 0.88 μm. This is factor ~9 larger than the thickness 100 nm of the ring electrode.

At z = 1.3 μm, the maximum potential decreased to 0.2 V, but the transverse spread reaches PE2 and PE3. As a result, even though $V_2 = V_3 = 0$, there is a finite phase shift for electrons that transmit through PE2 and 3. To evaluate this cross-talk effect, we calculated δU_{nk} given by the z-integration of the potential through the center trajectory of PEk when 1 V is applied to PEn. Using these quantities, the voltage ΔV_1 required for the π phase shift for electrons that transmit through PE1 with respect to PE2 and 3 when V_1 = 1 V and $V_2 = V_3 = 0$ V is given by $\pi / \{\sigma(\delta U_{11}-\delta U_{12})\}$, which is equal to $\pi / \{\sigma(\delta U_{11}-\delta U_{13})\}$. We found that $\delta U_{12} = \delta U_{32} = 0.16$ μm. As a result, we found ΔV_1 equal to 0.59 V. This is approximately 35 % smaller than experiment. Since the larger ΔV_1 suggests the shorter amount of $(\delta U_{11}-\delta U_{12})$, the disagreement between theory and experiment tentatively suggests that the potential spread in the z-direction above the ring electrode in the experiment was shorter than the calculated value in the above simulation. Such a reduction of the potential spread might be induced by the presence of surface charge over the device surface as a result of high-energy electron beam transmission, that could result in a partial screening of the potential. However, precise mechanism is unknown.

Since the transverse spread of the potential induced by PE1 is not uniform over PE2 and 3, the parasitic phase shift in PE2 and 3 are not uniform. In our device geometry, we found from the simulation that the edge-to-edge phase shift difference in PE2 and 3 across the diameter D = 1 μm of their apertures is equal to ~0.2π at V_1 = 1 V and $V_2 = V_3 = 0$ V, that was evaluated from the calculated potential distribution in the z-direction depicted in Fig. 10b. The first order effect of such nonuniformity is tilting of the wavefront of electrons transmitting PE2 and PE3 and the deflection away from PE1. The deflection angle is estimated to be on the order of $0.2\pi/(D/\lambda) \sim 10^{-6}$ rad, and its polarity is opposite to those observed in the experiment (see the next section).

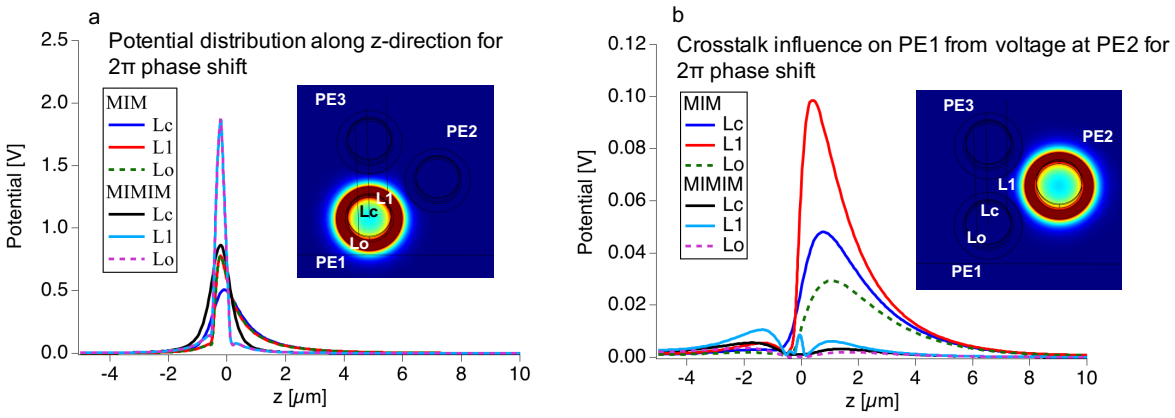

Figure 10: 1d potential distribution along z-direction at different line sections L_c, L_1 and L_o in phase shifting aperture 1 (PE 1) as shown in the inset images. L_c is passing through the center of PE1, L_1 is passing near the electrode edge of PE1 close to PE3 and L_o is passing through the electrode edge of PE2 at furthermost point from PE2 and PE3. (a) The graphs above show the

potential distribution along z from z = -5 to 10 μm for 2π phase shift. The equivalent voltage for MIM device = 1 V and MIMIM device = 2.3 V is considered in the simulation for comparison. The bottom electrode is located at z = 0 μm plane in both configurations. (b) The influence of crosstalk on adjacent electrodes is explained by showing the presence of potential distribution along PE1 while only PE2 is biased for voltage equivalent to 2π phase shift.

§4.4 Parasitic deflection of electron beam

In the experiment, we observed, in addition to the voltage-induced phase shift, deflection of the whole interference pattern, see Figs. 3, and 4, and Supplementary Video 1. The deflection of the interference pattern when V_n (n = 1,2,3) was varied was in the l_n-direction toward PEn for positive V_n, reverted for negative V_n, and the amount of the deflection was approximately proportional to V_n (within a factor of ~2 for all PEs). Therefore, we consider that the deflection was induced by the potential gradient caused by the contact-strip-part of the ring electrode.

To quantify the deflection angle, we note that, when V_1 was increased from 0 V to 2 V, the center of the beam shifted approximately by $S_{01}/2$ on the screen, where we define S_{01} equal to the distance between the central diffraction spot and the 1st order diffraction spot at V_1 = 0 V on the screen. Considering the relativistic wavelength λ = 2.5 pm for 200 keV electron beam and the center-to-center distance d = 1.8 μm between PEs, the angular distance corresponding to S_{01} is equal to λ/d = ~1.4 μrad. From this, we conclude that the deflection angle η at V_1 = 2 V is estimated to be equal to ~0.7 μrad (with the variation of a factor of ~2).

We compare this value with the ratio $\eta_{sim} = u_y/u_z$ of the transverse velocity u_y to the longitudinal velocity u_z, where u_y is evaluated by the following integral, and $u_z = 2.085\text{x}10^8$ m/s, (>> u_y) is given by the beam energy of 200 keV,

$$u_y \approx -\frac{e}{\gamma m_0 u_z}\int_{-\infty}^{\infty} dz F_y(z)\,; \tag{3}$$

where γm_0 is the relativistic electron mass (γ = 1.35), and m_0 is the electron rest mass.

§4.5 Electrostatic simulation of MIMIM device

To compare the phase shift characteristics of MIM device structure studied here with the MIMIM device as originally proposed by Boersch, wherein a second planar electrode at the same potential as the bottom electrode is added on top of the ring electrode, we next conducted the 3-dimensional electrostatic simulation. We assumed the same structure as our device for the ring electrode, insulator, and bottom electrode, and added a stack of a 0.2 um thick second insulator and a 0.1 um thick planar electrode above. The calculated potential distribution is shown in Fig. 10. As expected, the potential spread in the positive z-direction above the device was much reduced owing to the added planar electrode on the top at the ground potential. The potential variation along the electron trajectories at the middle and near the

edges of the aperture shows that the vertical spread was nearly a factor of 2 reduced, therefore approximately factor 2 higher bias voltage is required to achieve the same phase shift.

At the same time, the transverse spread of the potential was much reduced as shown in Fig. 11a and Fig. 11b. As a result, the cross-talk effect as well as the wavefront tilting effect became negligible (reduced by a factor of 5, therefore an order of magnitude smaller than the main phase shift through the biased PEs). Further, shielding of the contact strip of the ring electrodes is expected to eliminate the beam deflection effect as observed in the experiment and analyzed in section 4.5. These are important advantages for a device that integrates a large number of phase shifters.

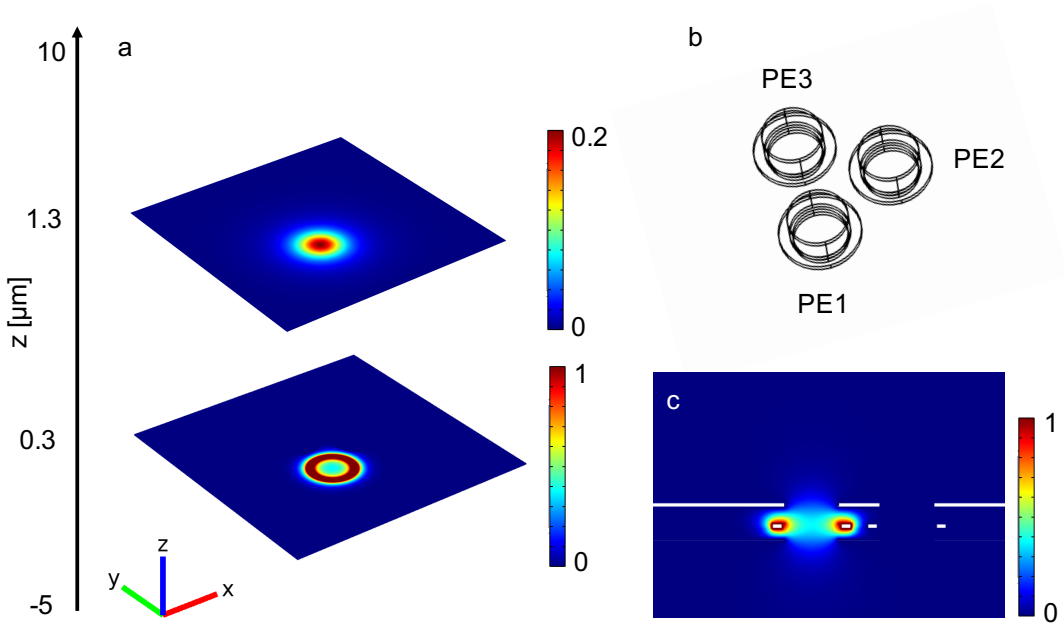

Figure 11: 3D electrostatic simulation of three aperture system metal-insulator-metal-insulator-metal (MIMIM) device with phase shifting element 1 (PE1), PE2 and PE3 is shown in (b). The entire system is confined within boundaries extending to (-4, -4, -5) µm to (4, 4, 10) µm in the rectangular coordinate system. The voltage distribution of the MIMIM device at z = 0.3 µm and z = 1.3 µm is shown in (a) when PE1 receives 2.3 V (potential values are normalized to maximum (red) for all images). From the cross-section of the MIMIM device in (c), it is evident that the crosstalk between two elements is significantly reduced compared to MIM device.

§4.6 Discussions

We evaluated the visibility v defined by $(I_{max}-I_{min})/(I_{max}+I_{min})$ of the interference[37] from the zero bias intensity profile for the V_1-scan dataset in Fig. 6a. By taking I_{max} equal to the average of the peak maximum and the peak value of the 1st order peak and I_{min} equal to the average intensity of the first dip of the intensity profile, we found the visibility values for the experiment and simulation, respectively, equal to v_{exp} = 0.49 and and v_{sim} = 0.54. Several possibilities can be thought of as the reason why the visibility is 10 % smaller in experiment. It is not likely that this is due to the insufficient coherence length of the electron beam. The application of ~2 V to the phase shifter element induced phase shift by 2π (one wavelength). Therefore, the longitudinal coherence length is unlikely to limit the visibility.

In fact, the estimated longitudinal coherence length[38] approximately given by $\lambda x E_0/(2\Delta E)$ is equal to ~$2x10^5$ λ = 0.4 μm, where ΔE ~ 0.5 eV is the energy spread of the electron beam emitted from the Schottky emitter, and much larger than λ. The transverse coherence length of the incident electron beam is more likely to be a limiting factor of the visibility. For quantitative comparison, it is desirable to conduct a separate but simultaneous measurement of the electron beam coherence.

Another possibility is the inelastic scattering of the electron beam during the propagation through the apertures of the phase elements, since the inelastically scattered electron would still reach the detector within the Airy disk radius (within the first order interference spots) but as a back ground, thereby increasing the intensity at the dips. We also note that the relative intensity of the 2nd order interference spots with respect to the 0th and 1st order interference spots is several times larger in experiment than in the simulation. In the latter, the sharp cut off of the intensity beyond the angles determined by the aperture diameter makes the 2nd spots extremely dark as the intensity profile of the simulated interference pattern in Fig. 6 shows. We found that this is difficult to ascribe to the smaller aperture dimeter or larger center-to-center distance than those estimated from SEM. This can partly be attributed to the finite angular divergence of the incident beam, even though the incident electron beam was nominally aligned as parallel and vertical on the device chip. To further optimize the interference visibility and to elucidate the visibility limiting mechanism is crucial for the feasibility of the large PE array device, especially their sizes. For that further experiments with the microscope alignment conditions such as different source aperture sizes and condenser lens adjustments, the in-situ evaluation of the transverse electron beam coherence length, or with the combination of the energy filtering[39] is required. However, further analysis and the application of such experimental methods are beyond the scope of the present work.

The visibility can also be reduced when the energy of the electron beams that transmitted through different apertures are slightly different: the energy difference should be within ~10^{-15} eV when the integration time of the image observation is in the order of 1 s[38,40,41]. This is especially the case when the phase shifter voltage is finite. In our MIM structure without the top shielding electrode, the potential decays slowly above the biased PEs as shown in the simulation in Figs. 9 and 10. In fact, the potential value in the simulation at the maximum z for such a device structure is finite, and the precise value is determined by the boundary condition as well as the domain size. Therefore, the experimental observation of the three-beam interference, especially at V_n's equal to ~2 V, and the fact that it is approximately identical to the case when V_n's was equal to 0 V shows that the electron energies of the three beams converged to a same value within ~10^{-15} eV when they propagated from the phase shifter device along the microscope column and reached to the detector. Nevertheless, as the simulation result shown in Fig. 11 indicates, when we apply the MIMIM device structure, the convergence of the electron beam energies within the small amount will be achieved within a few micron propagation distance from

the chip surface, which will be advantageous for applications, since it will allows for placing a sample close to the device.

§5 Summary and conclusion

Motivated by the exciting prospects for novel research in the field of molecular biology and material science for developing a next generation, holographic device of electron wavefront control with increased flexibility and reproducibility, we have fabricated a three element phase shifting device using electron beam lithography and reactive ion etching, a combination that is compatible with the scalable and high throughput device fabrication. The phase shift performance of the fabricated phase shifter device was tested in a 200 keV TEM, demonstrating an in-situ voltage controlled three-beam interference, including the rudimentary realization of a vortex beam. The analysis of the phase shift performance by way of comparing the intensity profiles with simulation showed that the phase shifter elements were capable to induce π-phase shift by applying ~0.9 V and this value was same for all the three PEs within 6 %. Phase offsets that vary among the PEs were observed but those were easily compensated by adjusting the bias voltages with the amount at most ~1 V. Comparing to a MIMIM device structure with two planar equipotential electrodes sandwiching the ring electrode surrounding the aperture, our MIM device without the top planar electrode was simple to fabricate and resulted in the effective electrode thickness of ~0.6 μm despite the fact that the ring-electrode-thickness was 0.1 μm with the total thickness-to-aperture diameter ratio of ~0.3. However, this at the same resulted in the deflection of the beams and a finite cross-talk between apertures up to ~20 % was predicted.

The simulation of the MIMIM device structure and its comparison with the MIM structure indicated the important advantages of the former, especially for a phase shifter array device with a large number of PE elements. Therefore, together with the development of the strategy for wiring individual ring electrodes, experimentally validation of these advantages of the MIMIM structure is an important next step of the research. This will increase the required voltage to achieve the 2π shift, however, the estimated factor 2 increase is much lower than the dielectric breakdown limit experimentally tested for our device with the insulator thickness of 0.2 μm. Alternatively, the ring electrode thickness can be increased, however with the potentially reduced device stability due to the increased accumulated stress for a device fabricated on the free-standing membrane as in the present work.

Acknowledgements

This work was partially funded by Swiss Nanoscience Institute, University Basel, Project No. P1505. We would like to thank Prof. Giulio Pozzi (University of Bologna, Italy) for his valuable insights and motivation for this work. We acknowledge Laboratory of Micro- and Nanotechnology (LMN), Paul

Scherer Institute, for supporting the device fabrication. We would also like to extend our thanks to Jana Lehmann (LMN-PSI, Switzerland) for her kind help with preparation of silicon nitride membranes.

References

[1] J. Verbeeck, H. Tian, and P. Schattschneider, Nature **467**, 301 (2010).
[2] B.J. McMorran, A. Agrawal, I.M. Anderson, A.A. Herzing, H.J. Lezec, J.J. McClelland, and J. Unguris, Science (80-.). **331**, 192 (2011).
[3] G. Guzzinati, L. Clark, A. Béché, R. Juchtmans, R. Van Boxem, M. Mazilu, and J. Verbeeck, Ultramicroscopy **151**, 85 (2015).
[4] R. Shiloh and A. Arie, Ultramicroscopy **177**, 30 (2017).
[5] E. Mafakheri, A.H. Tavabi, P.-H. Lu, R. Balboni, F. Venturi, C. Menozzi, G.C. Gazzadi, S. Frabboni, A. Sit, R.E. Dunin-Borkowski, E. Karimi, and V. Grillo, Appl. Phys. Lett. **110**, 93113 (2017).
[6] R. Cambie, K.H. Downing, D. Typke, R.M. Glaeser, and J. Jin, Ultramicroscopy **107**, 329 (2007).
[7] K. Schultheiss, F. Perez-Willard, B. Barton, D. Gerthsen, and R.R. Schröder, Rev. Sci. Instrum. **77**, 33701 (2006).
[8] J. Shiue, C.-S. Chang, S.-H. Huang, C.-H. Hsu, J.-S. Tsai, W.-H. Chang, Y.-M. Wu, Y.-C. Lin, P.-C. Kuo, Y.-S. Huang, Y. Hwu, J.-J. Kai, F.-G. Tseng, and F.-R. Chen, J. Electron Microsc. (Tokyo). **58**, 137 (2009).
[9] A.H. Tavabi, V. Migunov, C. Dwyer, R.E. Dunin-Borkowski, and G. Pozzi, Ultramicroscopy **157**, 57 (2015).
[10] S.-C. Chu, Y.-T. Chen, K.-F. Tsai, and K. Otsuka, Opt. Express **20**, 7128 (2012).
[11] G. Pozzi, P.-H. Lu, A.H. Tavabi, M. Duchamp, and R.E. Dunin-Borkowski, Ultramicroscopy **181**, 191 (2017).
[12] V. Grillo, G. Carlo Gazzadi, E. Karimi, E. Mafakheri, R.W. Boyd, and S. Frabboni, Appl. Phys. Lett. **104**, 43109 (2014).
[13] V. Grillo, G.C. Gazzadi, E. Mafakheri, S. Frabboni, E. Karimi, and R.W. Boyd, Phys. Rev. Lett. **114**, 34801 (2015).
[14] M. Uchida and A. Tonomura, Nature **464**, 737 (2010).
[15] V. Grillo, E. Karimi, G.C. Gazzadi, S. Frabboni, M.R. Dennis, and R.W. Boyd, Phys. Rev. X **4**, 11013 (2014).
[16] N. Voloch-Bloch, Y. Lereah, Y. Lilach, A. Gover, and A. Arie, Nature **494**, 331 (2013).
[17] R. Shiloh, Y. Lereah, Y. Lilach, and A. Arie, Ultramicroscopy **144**, 26 (2014).
[18] H. Boersch, Zeitschrift Für Naturforsch. A **2**, 615 (1947).
[19] E. Majorovits, B. Barton, K. Schultheiß, F. Pérez-Willard, D. Gerthsen, and R.R. Schröder, Ultramicroscopy **107**, 213 (2007).
[20] J. Verbeeck, A. Béché, K. Müller-Caspary, G. Guzzinati, M.A. Luong, and M. Den Hertog, Ultramicroscopy **190**, 58 (2018).
[21] A. Walter, S. Steltenkamp, S. Schmitz, P. Holik, E. Pakanavicius, R. Sachser, M. Huth, D. Rhinow, and W. Kühlbrandt, Ultramicroscopy **153**, 22 (2015).
[22] A. Walter, H. Muzik, H. Vieker, A. Turchanin, A. Beyer, A. Gölzhäuser, M. Lacher, S. Steltenkamp, S. Schmitz, P. Holik, W. Kühlbrandt, and D. Rhinow, Ultramicroscopy **116**, 62 (2012).
[23] C. Slinger, C. Cameron, and M. Stanley, Computer (Long. Beach. Calif). **38**, 46 (2005).
[24] Y. Igasaki, F. Li, N. Yoshida, H. Toyoda, T. Inoue, N. Mukohzaka, Y. Kobayashi, and T. Hara, Opt. Rev. **6**, 339 (1999).
[25] T. Latychevskaia and H.-W. Fink, Sci. Rep. **6**, 26312 (2016).
[26] N. Chattrapiban, E.A. Rogers, D. Cofield, I.I.I. Wendell T. Hill, and R. Roy, Opt. Lett. **28**, 2183 (2003).
[27] T. Matsumoto and A. Tonomura, Ultramicroscopy **63**, 5 (1996).
[28] Y. Zhang and P. Kruit, J. Vac. Sci. Technol. B Microelectron. Nanom. Struct. Process. Meas. Phenom. **25**, 2239 (2007).
[29] T.H.P. Chang, D.P. Kern, and L.P. Muray, J. Vac. Sci. Technol. B Microelectron. Nanom. Struct. Process. Meas. Phenom. **10**, 2743 (1992).
[30] P. Kruit, Microelectron. Eng. **84**, 1027 (2007).
[31] M. Esashi, A. Kojima, N. Ikegami, H. Miyaguchi, and N. Koshida, Microsystems Nanoeng. **1**, 15029 (2015).
[32] C. Klein, H. Loeschner, and E. Platzgummer, J. Micro/Nanolithography, MEMS, MOEMS **11**, 1 (2012).
[33] M. Ekberg, M. Larsson, S. Hård, and B. Nilsson, Opt. Lett. **15**, 568 (1990).
[34] V.A. Guzenko, A. Mustonen, P. Helfenstein, E. Kirk, and S. Tsujino, Microelectron. Eng. **111**, 114 (2013).
[35] E.R.-C. for M. and S. with E. (2016). F.T.G. F20, J. Large-Scale Res. Facil. **2**, **A77**, (2016).
[36] L. Reimer, in *Transm. Electron Microsc. Phys. Image Form. Microanal.* (Springer Berlin Heidelberg, 1984), p. 57.
[37] L. Mandel and E. Wolf, *Optical Coherence and Quantum Optics* (Cambridge University Press, Cambridge,

UK, 1995).
[38] J.C.H. Spence and J.M. Zuo, Ultramicroscopy **69**, 185 (1997).
[39] H. Lichte, Philos. Trans. Ser. A, Math. Phys. Eng. Sci. **360**, 897 (2002).
[40] V.D. D, H. Lichte, and J.C. Spence, Ultramicroscopy **81**, 187 (2000).
[41] J. Verbeeck, G. Bertoni, and H. Lichte, Ultramicroscopy **111**, 887 (2011).